Corrosion Science 50 (2008) 2646–2657

Contents lists available at ScienceDirect

Corrosion Science

journal homepage: www.elsevier.com/locate/corsci

Investigation of the corrosion behaviour of AA 2024-T3 in low concentrated chloride media

F.M. Queiroz [a], M. Magnani [b], I. Costa [a], H.G. de Melo [c,*]

[a] Energy and Nuclear Research Institute, IPEN/CNEN-SP, CCTM, São Paulo, Brazil
[b] Physical Chemistry Department, São Paulo State University, UNESP, São Paulo, Brazil
[c] Chemical Engineering Department, Polytechnic School of the University of São Paulo, CEP 05508-900, São Paulo, SP, Brazil

ARTICLE INFO

Article history:
Received 27 March 2008
Accepted 24 June 2008
Available online 8 July 2008

Keywords:
A. Aluminium
A. Intermetallics
B. EIS
B. SEM
B. TEM

ABSTRACT

Aluminium alloy (AA) 2024-T3 is an important engineering material due to its widespread use in the aerospace industry. However, it is very prone to localized corrosion attack in chloride containing media, which has been mainly associated to the presence of coarse intermetallics (IMs) in its microstructure. In this work the corrosion behaviour of AA 2024-T3 in low concentrated chloride media was investigated using microscopy and electrochemical methods. TEM/EDS observations on non-corroded samples evidenced the heterogeneous composition within the IMs. In addition, SEM observations showed that intermetallics with the same nominal composition present different reactivity, and that both types of coarse IMs normally found in the alloy microstructure are prone to corrosion. Moreover, EDS analyses showed important compositional changes in corroded IMs, evidencing a selective dissolution of their more active constituents, and the onset of an intense oxygen peak, irrespective to the IM nature, indicating the formation of corrosion products. On the other hand, the results of the electrochemical investigations, in accordance with the SEM/EDS observations, evidenced that IMs corrosion dominates the electrochemical response of the alloy during the first hours of immersion in the test electrolyte.

1. Introduction

The AA 2024-T3, due to its high-strength/weight ratio, is used in aircraft structures, rivets, hardware, truck wheels, screw machine products, and other miscellaneous structural application [1,2]. This material has a complex microstructure due to the addition of alloying elements and to the presence of impurities [1]. The precipitation sequence of the 2024 alloy consists in the formation of GPB (Guinier–Preston–Bagaryatsky) zones at room temperature, which can be classified as a short-range ordering of the Cu and Mg solute atoms [3]. After artificial ageing, these zones are dissolved and replaced by semi-coherent S″ (Al_2CuMg) precipitates. Finally, after longer exposure times, stable S (Al_2CuMg) phase are formed [3–5].

In this alloy, the alloying elements Cr, Mn, and Cu are generally added to control grain structure, weldability and corrosion resistance [6], and specifically Cu is added to improve mechanical resistance. This is achieved by the precipitation of small coherent particles dispersed through the whole matrix [2,7–10]. It is documented that, when in solid solution, Cu increases the localized corrosion resistance of the Al matrix [11]. However, Cu, together with other elements, also precipitates as bigger intermetallics (IMs), which attain high surface densities [12]. The electrochemical activity associated with these IMs is different from the matrix, and gives rise to localized corrosion phenomena [2,9–14]. Moreover, in their vicinity, the passive layer can be weaker and Cu depleted zones can be formed [10] leading to localized attack of the matrix.

Although it is generally accepted that the onset of localized corrosion of high strength Al alloys is associated with the presence of IMs [9,15], the initial steps of the mechanism is not established yet, mainly due to the IMs' small size, their heterogeneous dissolution [16–18], and to the fact that their reactivity depend on the electrolyte [9,16,19,20]. For the 2024 alloy, it is generally accepted that Al–Cu–Mg (S-phase) IMs are initially anodic and become cathodic to the matrix due to selective corrosion of their less noble constituents, namely, Al and Mg, leaving nobler Cu-rich remnants that provoke the corrosion of the adjacent matrix [2,10,15,16]. However, some authors also report cathodic dissolution of the matrix near these IMs due to pH rise [21], whereas others state that these IMs are never anodic relatively to the matrix [22].

Regarding the Al–Cu–Fe–Mn IMs, they are always considered nobler than the matrix [16,18,20,22–25] and, consequently, must sustain cathodic reaction. Several authors have described the dissolution of the matrix in their vicinity [12,18,26,27], and Cu deposition on them [12,24], enhancing galvanic activity. However, it has also been reported that they have heterogeneous composition

* Corresponding author. Tel.: +55 11 3091 2231; fax: +55 11 3031 3020.
E-mail address: hgdemelo@usp.br (H.d. Melo).

0010-938X/$ - see front matter © 2008 Elsevier Ltd. All rights reserved.
doi:10.1016/j.corsci.2008.06.041

[2,22,24,26,27], and undergo heterogeneous dissolution [15,18,22], that can also occur in the form of pitting corrosion [18]. Nevertheless, few authors have described that the Al matrix does not corrode in the vicinity of these IMs [10,26]. It has also been reported that they are less electrochemically reactive than others found in the microstructure of AA 2024-T3 [28].

In order to achieve better spatial resolution in the study of the localized corrosion phenomena associated to the presence of coarse IMs in the microstructure of high-strength Al alloys, a large number of high-resolution techniques have been employed to investigate the initial corrosion steps associated with these microstructural features. Some of these techniques are scanning Kelvin probe force microscopy (SKPFM) [18,20,24,29–31], *in situ* [18,20,24,29] and *ex situ* [20], atomic force microscopy (AFM), confocal laser scanning microscopy (CLSM) [16,28,30], fluorescence microscopy [23,32], near field scanning optical microscopy (NSOM) [31] and scanning electrochemical microscopy (SCEM) [29,32,33]. In the investigations specifically related to the corrosion of AA 2024-T3, most of the works have confirmed the anodic nature of the S-phase IMs, as well as their heterogeneous dissolution. However, some other specific important contributions can also be highlighted. *Ex situ* SKPFM has shown that both Al–Cu–Fe–Mn and Al–Cu–Mg IMs exposed to air have a higher Volta potential than the bulk matrix [18,20,24,29]. For these latter IMs this finding is in disagreement with the general accepted idea that they are anodic in relation to the bulk matrix. To explain this feature it was initially hypothesized that this difference was due to the presence of a modified oxide layer formed on these IMs, which, once removed, would change their character from cathodic to anodic [18,20,24]. Guillaumin et al. [29] gave important support to this hypothesis. Using Auger spectroscopy they evidenced the presence of a thin oxide layer above S-phase IMs that, once partially removed, caused a significant diminution in the particles Volta potential, turning them anodic to the matrix. However, it was also shown that the Volta potential could change according to the sputtering etching depth, indicating a compositional gradient, that some Volta potential differences was unrelated with compositional variations and that regions with different surface compositions can exhibit the same Volta potential [29]. All these works using high-resolution techniques have evidenced and confirmed the complex and heterogeneous electrochemical behaviour of the IMs in the AA 2024-T3 microstructure.

Transmission electron microscopy (TEM) essentially provides a high-resolution image of the microstructure of a thin sample. TEM is used extensively in both material science/metallurgy and biological sciences [34]. This technique has been employed to investigate the IMs found in the AA 2024-T3 microstructure mainly in works devoted to physical metallurgy characterization [3,35]. Wang and Starink [3], combining TEM and differential scanning calorimetry (DSC), identified two different types of S phase IMs, which formation were dependent on the thermal and mechanical history of the alloy. Gao et al. [35] used TEM and microanalysis to investigate the crystal structure of the main IMs found in the microstructure of AA 2024-T3, they reported the existence of minor elements in the composition of the S-phase particles, and suggested that Al–Cu–Fe–Mn–(Si) particles could be a modified form of Al_8Fe_2Si or $Al_{10}Mn_3Si$, whose crystal structure had been altered by the incorporation of the other elements. Moreover, for these latter particles, the authors reveal that, due to their various compositions, different crystal structures should be expected. Wei et al. [36] using the same alloy brand of Gao et al. [35] employed TEM to investigate particle-induced corrosion in high-strength Al alloys. In their approach they showed, through high-resolution images, the dissolution of the matrix around the IMs, and proposed some quantitative relations to calculate the current density due to particle-induced corrosion; however, they did not employed this technique to elucidate compositional variation within the IMs.

Within the framework of improving spatial resolution to gain a better insight on the role of the IMs in the corrosion of AA 2024-T3, traditional electrochemical techniques, namely polarization curves, have contributed through the use of microcells [11,17,23,26,27]. The main results have shown that IMs with the same nominal composition exhibit a high dispersion of pitting potentials [11,26,27], and that IMs, depending on their nature, sustain different rates of cathodic and anodic reactions [26]. It was also evidenced that IMs free zones present higher pitting potentials [11], and that interactions between neighbouring particles can lead to important changes in the local corrosion response [23]. However, when such approach is employed, it must be kept in mind that important electrolyte compositional changes may arise during the experiment, affecting the corrosion reaction rates.

EIS is a powerful tool to investigate the corrosion behaviour of coated and uncoated metallic materials. For aluminium alloys, only few works are available where it has been used to investigate localized corrosion phenomena [38,39]. In these works, it has been demonstrated that a diffusion-controlled process in the intermediate to low frequency (LF) domain characterizes pitting corrosion, which may be modelled using a Warburg element. Conde and Damborenea [39] reported that after 6 hours of immersion of an aged 2024-T3 alloy in 1 M NaCl + 10 mL of H_2O_2 30% solution, the impedance diagram is characteristic of purely activation controlled processes, typical of generalized corrosion, and that the change to the LF diffusion-controlled process occurs after longer immersion times. On the other hand, Ornek et al. [38], presenting data for tests longer than 24 h, verified the LF diffusion-controlled process attributable to pitting corrosion. However, the time scale that this phenomenon has been reported to occur, several hours of immersion in aggressive electrolytes [38–40], is inconsistent with the fast dissolution of IMs. Indeed, Schmutz and Frankel [18] reported that after slight AFM probe scratching S-phase IMs start to dissolve after only 4.3 min of immersion of AA 2024-T3 in 0.01 M NaCl [18]. So it is likely that the process the different authors [38,39] are detecting is the diffusion within large pits, indicating that, in their approach, EIS was insensitive to IM corrosion.

The aim of the present study is to investigate the electrochemical behaviour of AA 2024-T3 in low concentrated chloride medium, NaCl 1 mM. The electrolyte was chosen for two main reasons: firstly to restrain the interactions between IMs to a small solution volume, and secondly to avoid excessive corrosion of the bulk matrix, which may allow characterizing the effect of the IMs' corrosion in the electrochemical response. To perform the investigation, TEM was initially used to assess the internal microstructure of uncorroded IMs. SEM–EDS and phase shift interferometer microscopy (PSIM) were employed to characterize the corrosion evolution of IMs in samples previously characterized and then exposed to the test electrolyte at the open circuit potential (OCP). The electrochemical investigation was performed using anodic and cathodic polarization curves and electrochemical impedance spectroscopy (EIS). In the EIS diagrams the contribution of the electrolyte resistance to the high frequency (HF) response was mathematically treated in order to better highlight the contributions of the fast phenomena to the electrochemical process. Although the electrochemical behaviour of this alloy has already been extensively investigated, as far as we are concerned, none of these investigations were performed in electrolytes with such low concentration of NaCl; moreover, the treatment of the HF frequency region of the EIS diagrams is an original approach allowing to better evaluate the response of the fast processes in the overall electrochemical response.

Table 1
Mean composition of the intermetallics and standard deviation associated with each element

Intermetallic 1 (49)			Intermetallic 2 (12)		
Element	At.%	Std. deviation	Element	At.%	Std. deviation
Al	59.95	5.25	Al	76.32	2.93
Cu	19.49	2.15	Cu	12.99	3.30
Mg	20.40	3.22	Fe	5.63	1.43
			Mn	4.36	1.70
			Si[a]	0.19	0.19

In parenthesis the number of IMs analysed.
[a] Some of the particles presented a Si content of 0%.

2. Experimental

An AA 2024-T3 sheet provided by a Brazilian industry with a nominal composition (weight%): Cu 4.86, Mg 0.59, Mn 0.7, Fe 0.28, Si 0.19, Ti 0.1 and balance of Al was used as working electrode (WE). Prior to the electrochemical measurements the samples were embedded with epoxy resin, their external surface ground up to 4000 grit emery paper, and subsequently polished with diamond paste 3 and 1 μm (alcohol lubricated). During surface treatment, the samples were sonicated for 15 min in deionised water when changing from grinding to polishing, and extensively washed with deionised water each time the ground paper or polishing cloth was changed.

All the electrochemical measurements were performed using a conventional three-electrode cell at room temperature in aerated NaCl 1 mM solution. A saturated calomel electrode (SCE) was used as reference, which was connected to the working solution through a Luggin capillary. A platinum network was used as auxiliary electrode.

Anodic and cathodic polarization curves were independently obtained from the OCP at 0.5 mV s^{-1} scan rates, after different immersion times. The experimental set-up consisted of a Solartron 1287 electrochemical interface coupled to a PC and controlled by the software Corrware®. This same set-up coupled to a Solartron 1250 frequency response analyser (FRA) was used to obtain the EIS diagrams, which were performed at the OCP in the frequency range from 10 kHz to 10 mHz, with a perturbation amplitude of 15 mV (rms), and an acquisition rate of 10 points per decade.

SEM–EDS analyses were performed using a LEO 435 VP microscope with an incident beam of 15 keV. The observation of the as-polished surface of different samples revealed the presence of two main types of coarse IMs: the round-shaped Al–Cu–Mg and the irregular Al–Cu–Fe–Mn–(Si). EDS surface mapping showed that the area fraction covered by IMs was approximately 4%. Table 1 presents the mean composition of the IMs and the standard deviation associated with each element.

Transmission electron microscopy (TEM, Philips CM30 instrument operating at 200 kV) was used to assess the internal microstructure of the IMs. The samples were cut into disks with 3 mm in diameter (South Bay Technology, SBT, SONICUT 380) and ground down to 20 mm (Dimple grinder, SBT 515) before ion milling (Ion Beam Milling System, BAL-TEC Model RES 010). TEM observation could then be performed on the thinnest areas of the sample, typically less than 100 nm thick. Energy dispersive spectroscopy (EDS) was obtained with a digital spectrometer (Princeton Gamma Tech, Model PRISM).

Phase shifting interferometric microscopy (PSIM) was employed to follow the dissolution of specific intermetallics after exposure to the test electrolyte. The method is based on classical interferometry and lies in the acquisition of four images of the same surface with a difference of $\lambda/4$ in optical path length between consecutive images [41].

3. Results and discussion

3.1. Microstructural characterization

As evidenced in the introductory part of this work, for AA 2024-T3, IMs with the same nominal composition may corrode at different rates. This has been frequently associated with heterogeneities within these particles, however, in none of the consulted works unequivocal analytical proofs were offered about this matter. TEM was used in order to improve understanding about the microtexture and composition of the two main types of IMs usually found in this alloy, namely: Al–Cu–Fe–Mn–(Si) and Al–Cu–Mg (S phase). The overall results evidenced significant compositional differences within most of the analysed particles, confirming their expected heterogeneity. A selection of our more important findings is reported hereafter.

Fig. 1A shows the micrograph of an IM, identified by EDS as Al–Cu–Fe–Mn–(Si). The IM corresponds to the darker area in the centre of the image. Fig. 1B is a dark field (DF) image obtained in a magnified region within the IM, exhibiting Moiré patterns. However, these Moiré modulations are not present in the whole IM, and several regions, delimited by curved interfaces, lack completely this pattern. This must be due to some crystalline variation, probably due to some local compositional change. EDS spectra recorded on various points inside this IM (spots "a" to "d" in Fig. 1B), especially in and out of the Moiré region, showed indeed some discrepancies. As reported on Fig. 1C: spectrum "b", corresponding to an area located out of the Moiré pattern, shows comparatively higher Cu and Fe contents, than the "a" spectrum, recorded on the Moiré region. On the other hand, the "c" and "d" areas contain intermediate amounts of Cu and Fe. These latter results could be due to a mixing effect, if the spectra were recorded on the interface of both areas.

According to the literature, the light and dark bands visible in Fig. 1 is suggestive of Moiré patterns formed by double diffraction between an overlying and an underlying layer of slightly different interplanar spaces [42], in this case the texture observed is due to the superposition of the IM matrix with smaller precipitates. The patterns exhibited in Fig. 1B are similar to those presented in the work of Munitz et al. [37]. These authors [37] proposed the existence of some segregation in their IM, which would be at some intermediate stage in the transition from the (Fe,Mn,Cu)Al_6 non-equilibrium phase to the Al_7Cu_2Fe equilibrium phase. In their work, Munitz et al. [37] suggested that these segregations could be associated with Mn excess within the particle.

Fig. 2A presents a TEM image of another Al–Cu–Fe–Mn IM with its associated diffraction pattern, Fig. 2B. The magnified image of the small particle within the circle in Fig. 2A is presented in Fig. 2C, and its associated diffraction pattern is showed in Fig. 2D. Fig. 2B and D suggest that both regions are monocrystalline with superstructure due to the different intensities of modulation, and indicate the co-existence of regions with different microstructure within the same IM. Also, it was observed by EDS that the smaller IM of Fig. 2C presents lower iron content when compared with the bulk of the IM.

Fig. 3A presents the TEM bright field image of an S-phase IM, with its associated diffraction pattern, Fig. 3B. The latter image reveals the presence of a second phase within the crystalline IM, which is associated with the well-defined rings, indicating that it must be an amorphous or nanocrystalline phase. This other phase is probably associated with the small bright points of Fig. 3A. Indeed, high-resolution EDS analyses performed in few of these points showed that they are richer in Cu and poorer in Mg than the

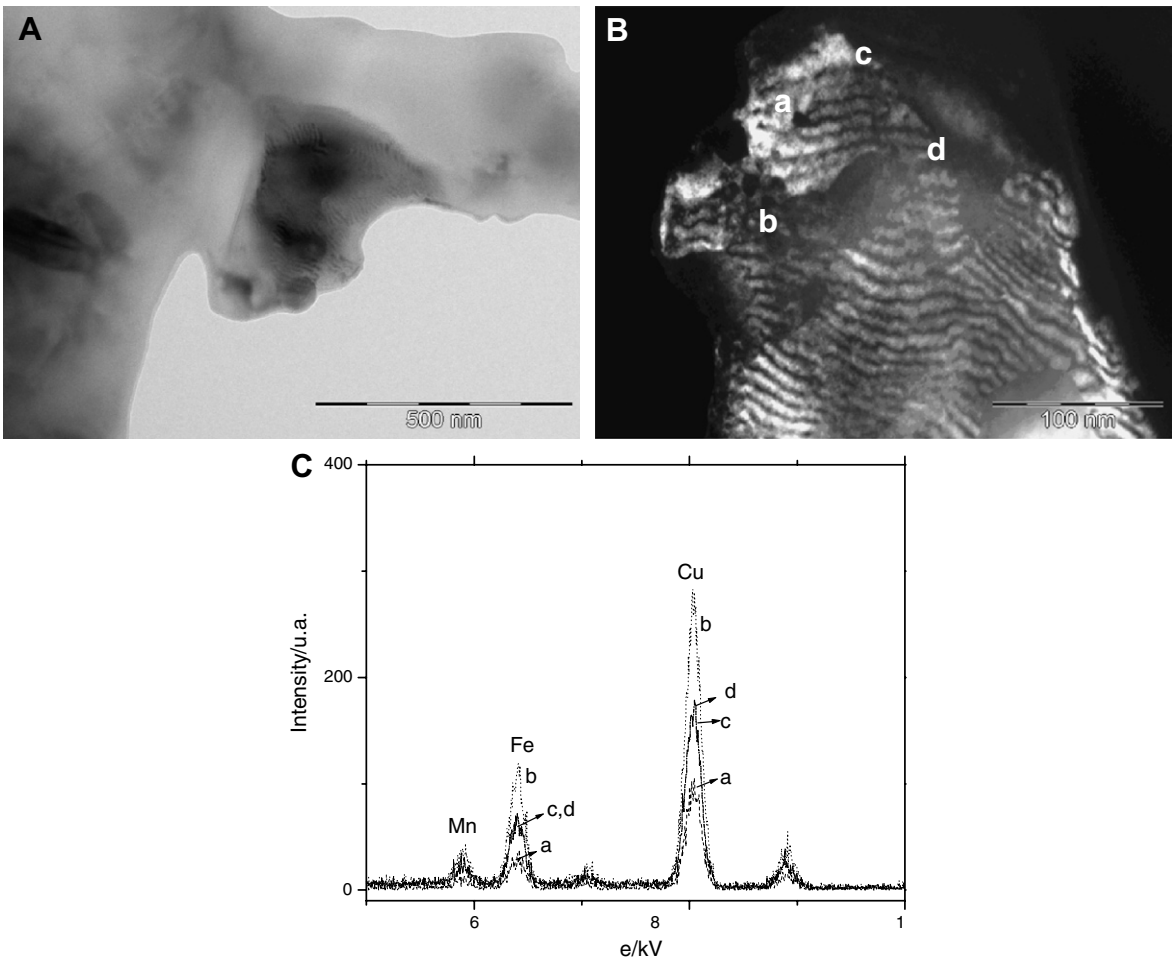

Fig. 1. (A) TEM micrograph of a Al–Cu–Fe–Mn IM; (B) TEM image of a selected region (A); (C) EDS spectra associated to the spots identified in (B).

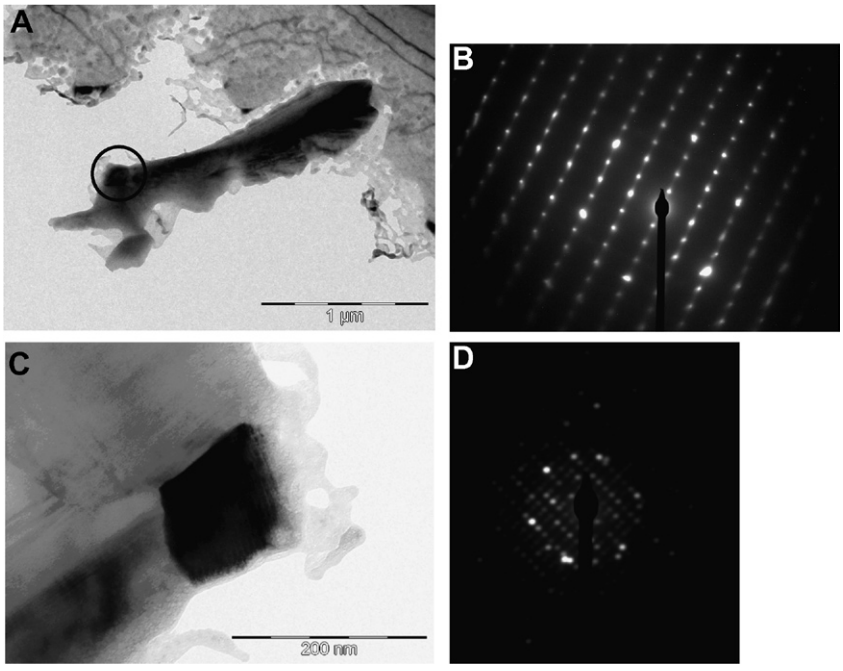

Fig. 2. (A) TEM micrograph of a Al–Cu–Fe–Mn IM, (B) diffraction pattern associated with the image in (A), (C) TEM micrograph of a Al–Cu–Fe–Mn IM insert of polycrystalline region within an Al–Cu–Fe–Mn IM, and (D) diffraction pattern associated with the image in (C).

bulk of the IM. Magnified image of the IM in Fig. 3A, not presented here, also revealed the existence of small areas containing Moirés patterns, which could be an indication of the co-existence of non-equilibrium phases inside this IM.

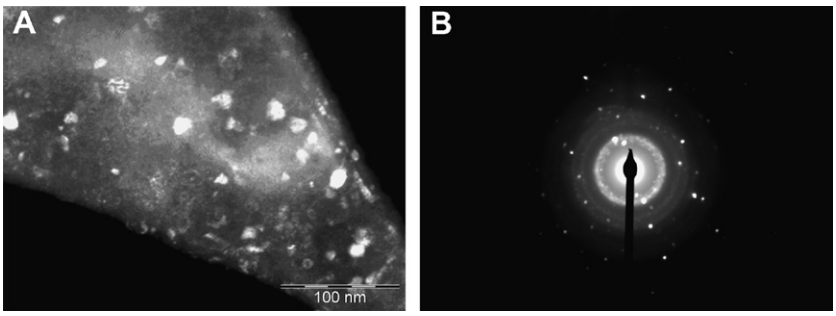

Fig. 3. (A) Bright field image of a S phase (Al–Cu–Mg) IM; (B) diffraction pattern associated with (A).

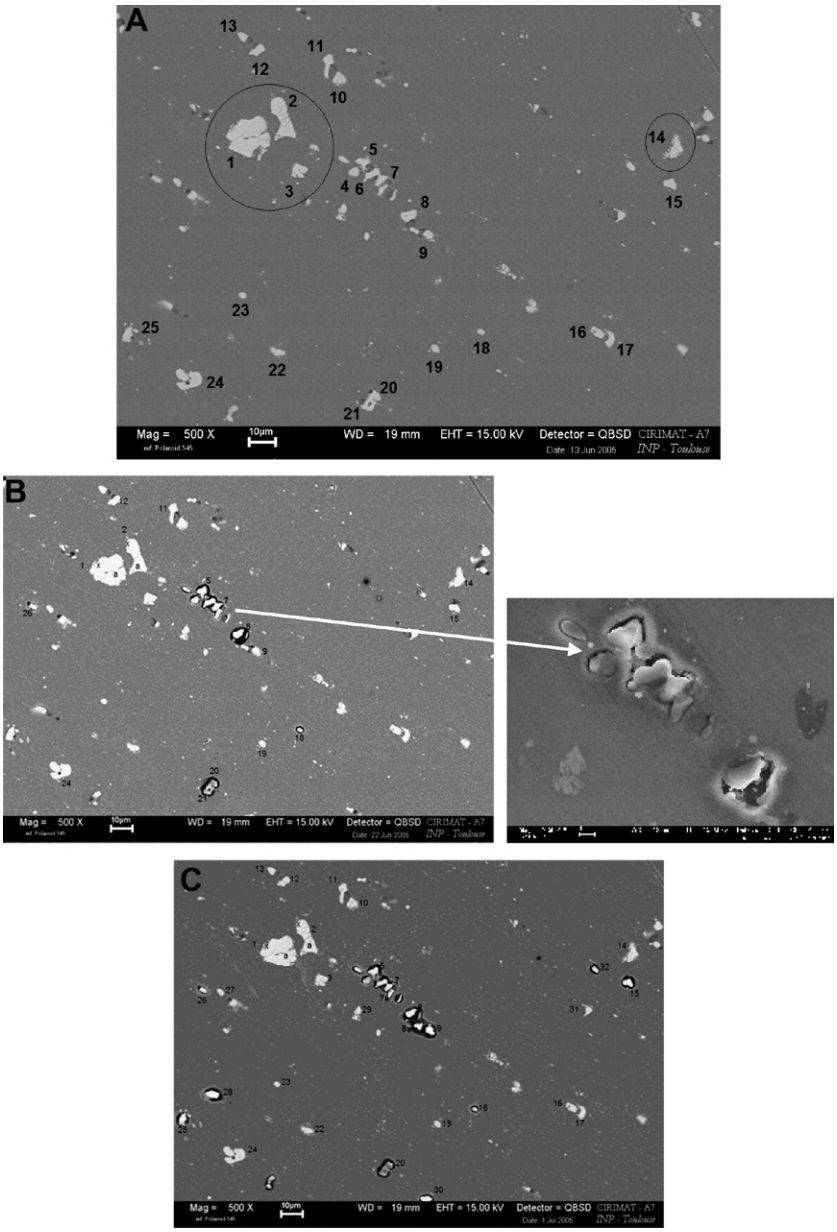

Fig. 4. SEM micrographs of AA 2024-T3 (A) polished sample; (B) after 4 h immersion in NaCl 1 mM; (C) after 8 h of immersion in NaCl 1 mM. Inset: detail of corroded S-phase IMs.

The TEM survey also revealed the presence of small rod shaped (most of them with *c.a.* 100–200 nm) Al–Cu–Mn precipitates almost homogeneously distributed within the bulk of the alloy. However, depletion zones of these particles were found around some coarse

Al–Cu–Fe–Mn and Al–Cu–Mg IMs. It has been reported in the literature [10] that these depleted zones can be more susceptible to localized corrosion phenomena.

A polished sample was immersed in the 1 mM NaCl test solution during two consecutive periods of 4 h (total of 8 h of exposure), and the morphology and composition of several IMs of the same region was evaluated by SEM–EDS before and after immersion in the test electrolyte. The micrographs are presented in Fig. 4A–C, for the as polished, 4 h and 8 h tested sample, respectively. The Al–Cu–Fe–Mn–(Si) IMs are marked as 1, 2, 3 and 14, while all the others labelled IMs are of the Al–Cu–Mg type. Fig. 4B and C clearly show that, in the selected region, the corrosive attack is concentrated near the S-phase IMs. On the other hand, Al–Cu–Fe–Mn–(Si) IMs neither showed any significant change during the exposure period (also confirmed by EDS analysis), nor the matrix was affected at their vicinity. Moreover, it can be also verified that the corrosion behaviour of the S-phase IMs is inhomogeneous, in this manner some particles were heavily attacked after only 4 h of exposure (IMs 4–8) while others were not apparently affected by any corrosion process after 8 hours (IMs 10, 11, 15–17, 24).

From Fig. 4B and C it is possible to verify that the more heavily attacked S-phase particles (4–9) are located near the bigger Al–Cu–Fe–Mn–(Si) IMs (1–3). In addition, the matrix apparently suffered corrosion in this region, as shown in the insert of Fig. 4B, indicating local electrochemical activity of the attacked IMs towards the matrix.

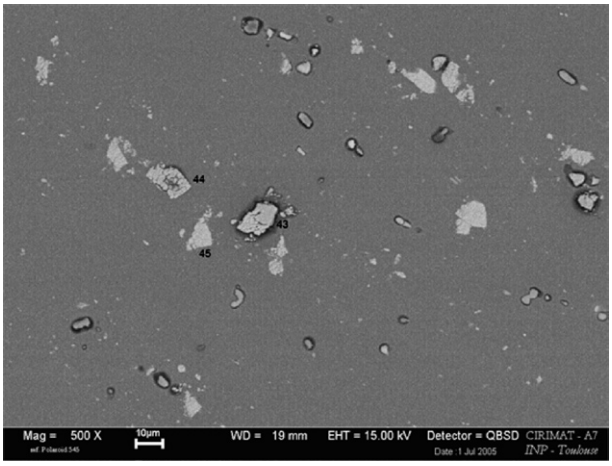

Fig. 5. SEM image of another region of the sample presented in Fig. 4 evidencing the corrosion of clustered Al–Cu–Fe–Mn–(Si) IMs.

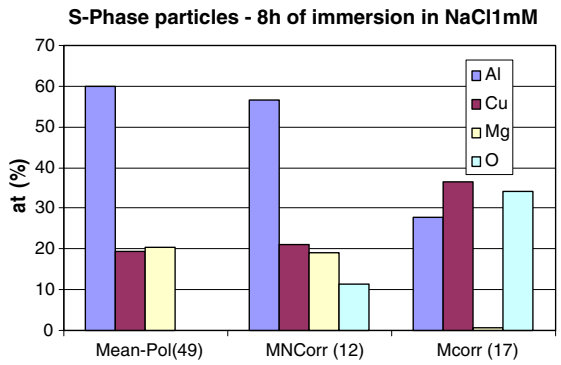

Fig. 6. Compositional evolution of corroded (Mcorr) and non-corroded (MN-corr) S-phase particles after 8 h of immersion in 1 mM NaCl solution. Mean-Pol represents the mean composition of the particles in the non-corroded state. IMs issued from different samples. In parenthesis the number of analysed particles.

Even though in the region presented in Fig. 4 no corrosion was associated to the presence of Al–Cu–Fe–Mn–(Si) IMs, this was not true for the whole exposed surface. Fig. 5 shows another region of the same sample used to acquire the images of Fig. 4 where a great number of clustered Al–Cu–Fe–Mn–(Si) IMs are present. The image was obtained after 8 h of immersion in the test solution. It is possible to see that, besides the expected corrosion of the round-shaped Al–Cu–Mg, there is an intense corrosion activity near several of the nobler clustered IMs, which had their less noble constituents (Al and Mn) selectively attacked.

Fig. 6 presents the compositional evolution, determined by EDS analyses, of several S-phase particles (issued from different samples) after 8 h of exposure to the 1 mM NaCl solution. In the diagram, the mean composition after the tests of corroded (Mcorr) and non-corroded (MN-Corr) particles are represented. In addition, as a reference, the mean composition of these same particles in the as-polished sample (Mean-Pol) is also given. This figure shows that, after the test period, non-corroded particles present almost the same composition as the as-polished ones, with the difference that few of these particles presented an oxygen peak. On the other hand, a strong oxygen peak was associated to all the corroded IMs and, also, a strong diminution in the amount of Al was detected, whereas Mg almost disappeared. These results suggest that the oxygen peak detected on the non-corroded particles might be due to an incipient corrosion process not noticeable through SEM imaging.

A similar response was observed when Al–Cu–Fe–Mn–(Si) IMs were concerned. When some corrosive activity was visualized at their vicinity, an important diminution of the EDS peaks intensities associated with Al was noted, together with an increase of the peak intensity related to Cu, indicating the onset of selective corrosion process. Besides, the intensity of the peaks ascribed to Mn decreased while those ascribed to Fe increased. Also for these IMs, an intense oxygen peak was detected in altered particles, which was always associated to the development of trenches around them. Non-corroded particles did not show either compositional change or oxygen peaks, and no corrosion of the matrix was detected around these particles by SEM observations.

The use of very low concentrated chloride solution was advantageous for the analysis of the interaction between the matrix and the IMs, as, for the test periods (4 and 8 h), no attack of the matrix was seen far from the IMs, except for the detachment/dissolution of minor particles. In addition, little interaction seems to have taken place among particles situated further apart.

The images of Fig. 4 show that the more intense localized attack occurred in the S-phase IMs near a cluster of Al–Cu–Fe–Mn–(Si) IMs. In a recent work, Leblanc and Frankel [23], using microcells, verified that the proximity of more noble Al–Cu–Fe–Mn–(Si) intermetallics to S-phase particles enhances the corrosive attack of these latter, since they act as efficient cathodic sites for reduction reactions. According to these authors, the pitting corrosion mechanism is dramatically affected by increase in the Al–Cu–Fe–Mn particles area ratio and can change from dissolution of Al_2CuMg inclusions to matrix attack, as this ratio increases. This corrosion mechanism can be likely applicable to the observed region but no straightforward conclusion can be drawn due to the inhomogeneous corrosion response of the S-phase particles, since, as observed in Fig. 4B and C, relatively isolated S-phase particles (18, 20, 25, 28) also corroded. This is in contradiction with Leblanc and Frankel [23] findings that verified neither the corrosion of the matrix nor that of the S-phase particles in regions where Al–Cu–Fe–Mn IMs were absent. In addition, the attack of the matrix adjacent to the S-phase particles seems to be driven by a local potential difference once it is concentrated in the vicinity of the Cu-enriched IMs. This latter feature is in accordance

with the anodic mechanism proposed by several authors for the dissolution of the matrix of 2024 alloys.

In accordance with literature [28], throughout this work it was verified that Al–Cu–Fe–Mn–(Si) IMs were more stable than S-phase particles. The data of Table 1 show that despite their larger sizes, the Al content in the Al–Cu–Fe–Mn–(Si) IMs is higher than in S-phase particles. This means that they are intrinsically richer in Al, since EDS results are less influenced by emissions from the bulk matrix, and this could explain the lower reactivity of these IMs. However, in this study, several of these IMs were heterogeneously corroded, and trenches were formed in the matrix around corroded particles, as shown in Fig. 5. In their work with microcells, Leblanc and Frankel [23] observed accelerated attack of the 2024-T3 matrix in NaCl solution in regions where only Al–Cu–Fe–Mn–Al IMs and the matrix were exposed; however, these authors did not reported the corrosion of the IMs. The authors [23] also observed that the higher the surface area ratio occupied by the IMs, the heavier was the corrosion attack of the adjacent matrix, which is in agreement with the results of the present study. Ilevbare et al. [16] verified neither compositional change nor trenches near Al–Cu–Fe–Mn IMs after they have been exposed to sulphate/chloride solution, however, this can be probably attributed to the passivating action of sulphate ions in relation to Al, even though corrosive attack of the IM should be expected [15].

Considering regions of the sample where S-phase particles were relatively further apart from the Al–Cu–Fe–Mn–(Si) IMs, like the one presented in Fig. 5, the incidence of corrosion in and around clustered Al–Cu–Fe–Mn–(Si) particles was higher than in isolated ones, confirming the area effect already proposed by Leblanc and Frankel [23]. However, in the great majority of these clusters, within the time span of this investigation, some of the IMs were heavily corroded while others were not. Taking into account the low conductivity of the electrolyte used in this work, and the fact that isolated Al–Cu–Fe–Mn–(Si) IMs seem to be more stable, these are evidences that some kind of interaction may occur between Al–Cu–Fe–Mn–(Si) particles themselves. Conversely, when these particles (clustered or isolated) were close to S-phase ones they were seldom corroded, indicating some kind of cathodic protection effect.

The common features of the results obtained in the present work were the modifications of the IMs composition, namely diminution of the EDS peaks intensity of their more active constituents and the onset of an intense oxygen peak, for all the particles that had their corrosion behaviour followed with immersion time, no matter their original composition. On the other hand, for IMs in which no apparent corrosion activity, either of the matrix or of the IM itself, was perceived, little or no compositional change was detected, and the oxygen peak was either absent or present as a shallow peak. From the experimental results obtained, the following sequence of events can be proposed for the localized corrosion attack near IMs:

a. Selective corrosion of the more active constituent of the particles, leaving a cathodic remnant.
b. Formation of oxygen containing products, probably issued from the corrosive process within the IMs.
c. Localized attack of the surrounding matrix driven by the potential difference between it and the oxide-covered ennobled particle, leading to the formation of trenches.

This mechanism is effective and independent on the IM nature, even though it was evidenced that S-phase IMs are much more active than their Al–Cu–Fe–Mn–(Si) counterparts. Finally, it is important to emphasize that, within the detection limits of the techniques employed, and for a great number of analyses carried out: corrosion activity was only detected when compositional changes took place within the IM.

In order to investigate the internal selective attack on the IMs, probably driven by the internal compositional variation as suggested by TEM, a polished sample of the alloy 2024-T3 was observed by PSIM after different immersion times in the NaCl 1 mM test solution. Either due to differences in hardness between the particles and the matrix, or because they were less corroded during the polishing procedure, less material was removed from the IMs making them to protrude. In this fashion, they were readily visible in the interferometric image. Moreover, their particular shapes facilitated the identification of their nature, even without performing EDS analyses. Figs. 7 and 8 present the images of an Al–Cu–Fe–Mn–(Si) and of an Al–Cu–Mg IM, respectively.

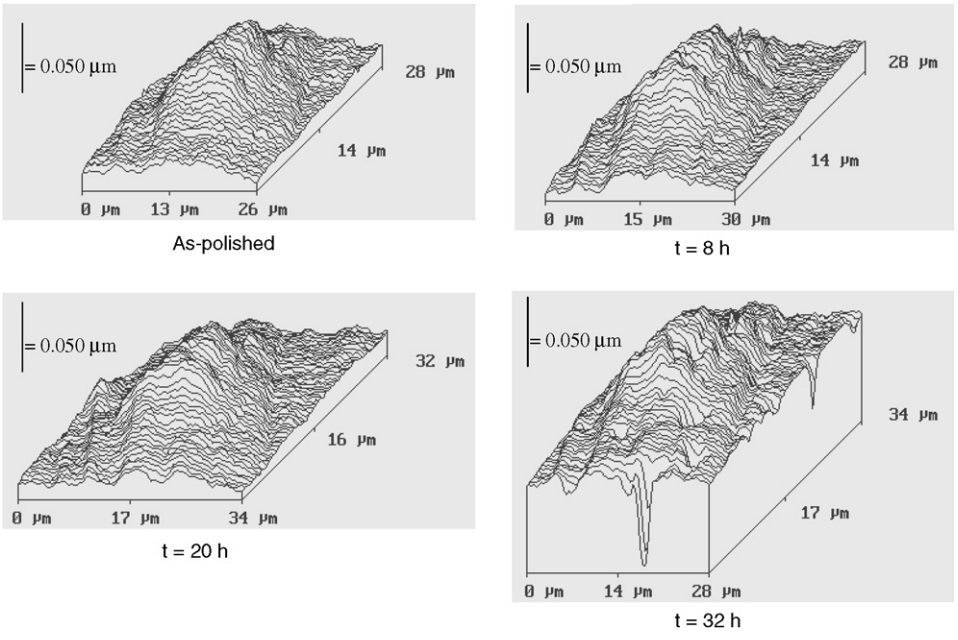

Fig. 7. Corrosion of a Al–Cu–Fe–Mn–(Si) IM in the 1 mM NaCl solution followed by phase shifting interferommetric (PSIM) images.

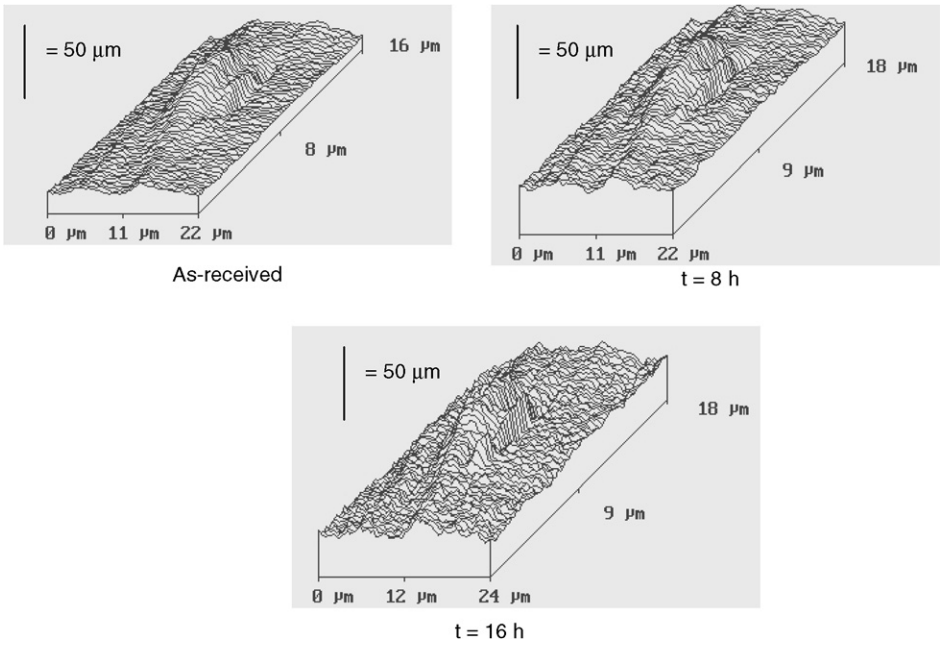

Fig. 8. Corrosion of a *S*-phase IM in the 1 mM NaCl solution followed by phase shifting interferommetric (PSIM) images.

It is possible to see in Fig. 7 that the contours of the IM become more irregular as its contact period with the test electrolyte increases. After 8 h of test, the onset of internal attack is detected, as seen on the back of the image and on its centre where more irregularly shaped contours are visible. The contours of the matrix nearby also became more irregular, indicating that it has undergone corrosive attack, probably due to IM ennoblement. This phenomena sequence is more clearly visible in the image obtained after 20 h of test. Finally, after 32 h, the presence of few deep pits was detected in the matrix nearby, indicating the onset of localized corrosion. The same phenomena sequence was verified for the S-phase particle depicted in Fig. 8. Also for this IM, after longer exposure periods, deep pits developed in the neighbouring matrix; however, due to the size of the acquired image (the pits were too profound) it was not possible to present them. It must be emphasized that the corrosion attack of the matrix was more intense near the S-phase particles, which can be attributed to the more cathodic nature of the Cu-rich remnant, and this hindered PSIM observations near these particles for longer test periods.

3.2. Electrochemical characterization

Two different OCP plateaus were observed for the polished alloy, at approximately −540 mV/ECS and −430 mV/ECS, and this was obtained for several samples with very good reproducibility. Anodic polarization curves showed that these different responses were due to a stronger polarization of the anodic processes in the samples with higher OCP. As shown in the microstructural investigation, the IMs present heterogeneous corrosion behaviour; this can explain the dissimilar electrochemical responses exhibited by different samples. However, as most of the samples presented lower potential, only the results associated with them are discussed here, even though the corrosion behaviour with immersion time was similar for both of them.

Fig. 9 presents anodic and cathodic polarization curves for AA 2024-T3 in 1 mM NaCl after different immersion periods. For increasing immersion times, the results show a net and a slight depolarisation of the cathodic and anodic branches, respectively. In the anodic curves, neither a passive current plateau nor a pitting potential was defined, indicating that active corrosion processes

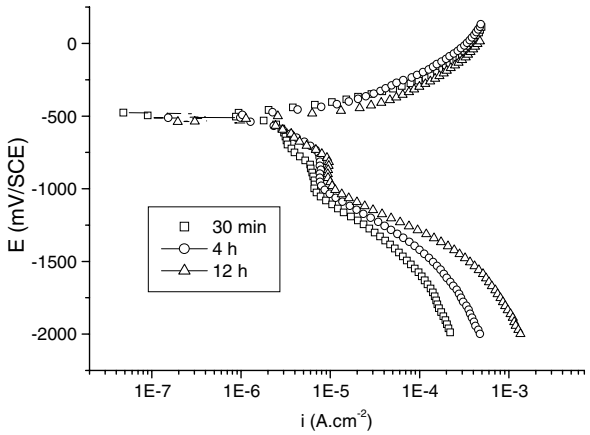

Fig. 9. Anodic and cathodic polarization curves for AA 2024-T3 in 1 mM NaCl solution.

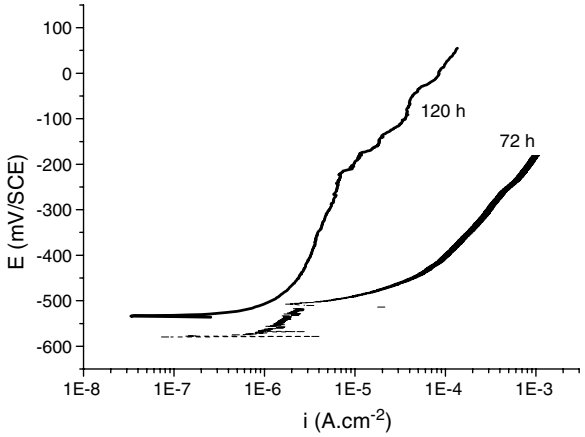

Fig. 10. Anodic polarization curves for AA 2024-T3 in 1 mM NaCl solution after 72 and 120 h of immersion.

take place in a short immersion time, which is in accordance with results reported by Ilevbare et al. [16] for this alloy in 0.5 M H_2SO_4 + 5 mM NaCl, and by Schmutz and Frankel in NaCl solution [18]. Moreover, the OCP curves showed no potential spikes, even after 12 h of exposure, indicating no passive layer breaking down. Recent investigations, performed with microcells in regions free of IMs of high resistance Al alloys, showed that the pitting potentials of these regions were much higher than those associated with particles bearing regions [16]. Based on the experimental evidences, the literature data and the SEM/EDS observations previously reported, it is proposed that the observed anodic behaviour is mainly due to the activity within the IMs and at their vicinity. Aiming to further investigate this issue, anodic polarisation curves were obtained after 3 and 5 days of immersion, the results are presented in Fig. 10. In both curves a clear passive range is established, which increases and becomes more defined as immersion time augment. This response would be associated to the bulk passive alloy, and would be effective only after the anodic activity of the IMs has been minimized due to their enrichment in their more noble constituents or detachment, giving support to our previous hypothesis to explain the earlier anodic behaviour. It is worth to emphasize that the proposed sequence of events is only valuable in extremely low aggressive electrolytes, where the bulk alloy is only slightly etched by the presence of aggressive species and pitting phenomena is not extremely favoured.

On the other hand, in accordance with literature data [2,10,12,15,16,24], the microstructural characterization showed that corrosion of the IMs leads to their enrichment in their more noble constituents, and this, in turn, can activate the cathodic reaction, leading to an autocatalytic process as proposed by Yasakau et al. [43]. The depolarisation of the cathodic branch can be explained by Cu enrichment in the particles, since the overpotential for the O_2 and H^+ cathodic reactions are lower on Cu than on oxidized Al surface [26].

Fig. 11A represents the impedance response, as Bode diagram, for the AA 2024-T3 after 45 hours of immersion in the test electrolyte. In this diagram, only two time constants are perceptible: one in the medium frequency (MF) range, and another in the low frequency (LF) region. Fig. 11B shows the plot of the imaginary impedance vs. frequency for the diagram depicted in Fig. 11A. In this illustration, the occurrence of three time constants is indicated (the one in the MF range is emphasized). In a recent work, Jorcin et al. [44]

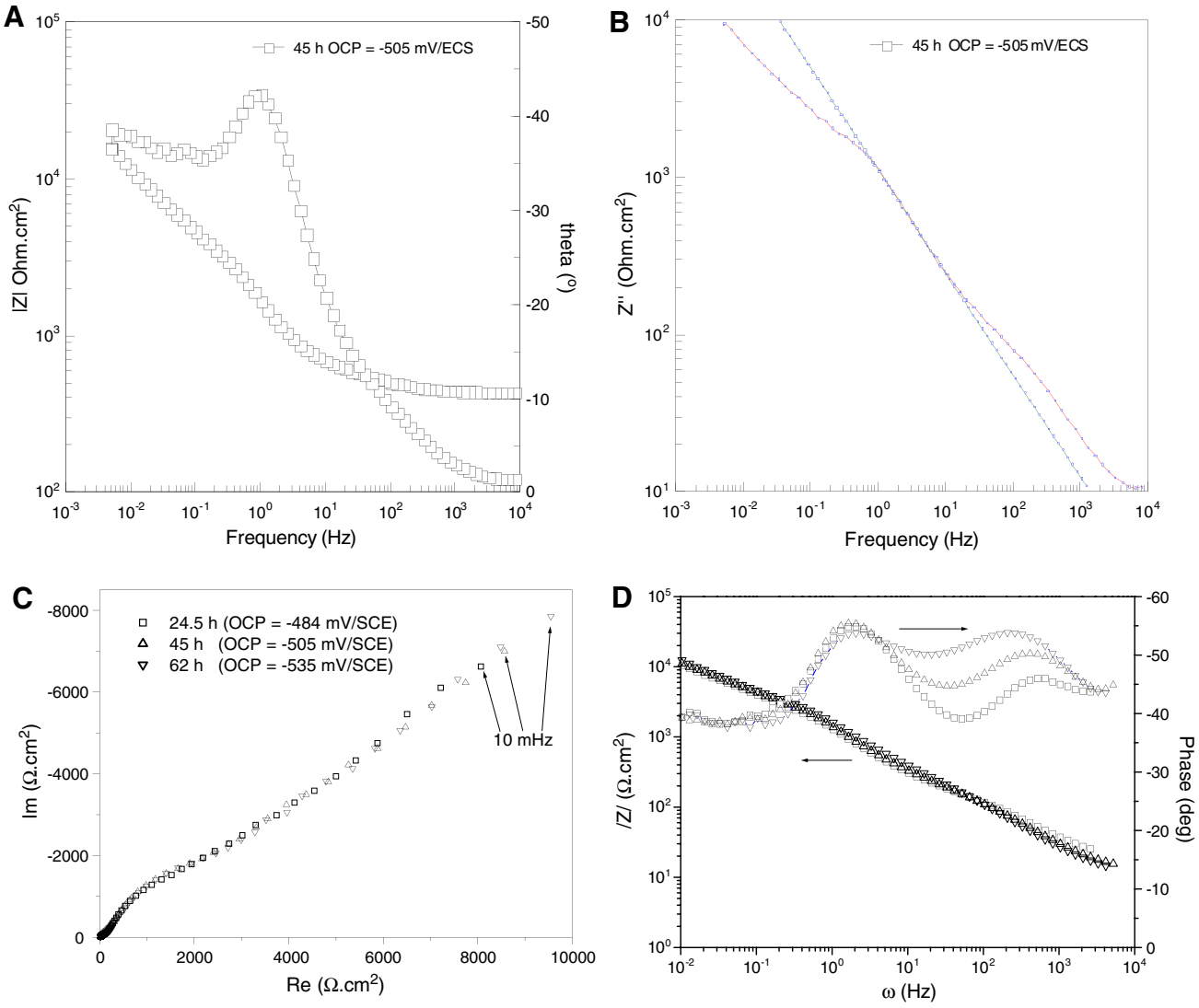

Fig. 11. (A) Untreated Bode phase angle diagrams for AA 2024-T3 alloy in 1 mM NaCl solution; (B) imaginary part of the impedance for the diagram presented in figure (A) evidencing the existence of three time constants; (C) Nyquist plots for AA 2024-T3 after different immersion times in 1 mM NaCl solution; (D) Bode diagrams corresponding to the data of (C), data without the electrolyte resistance.

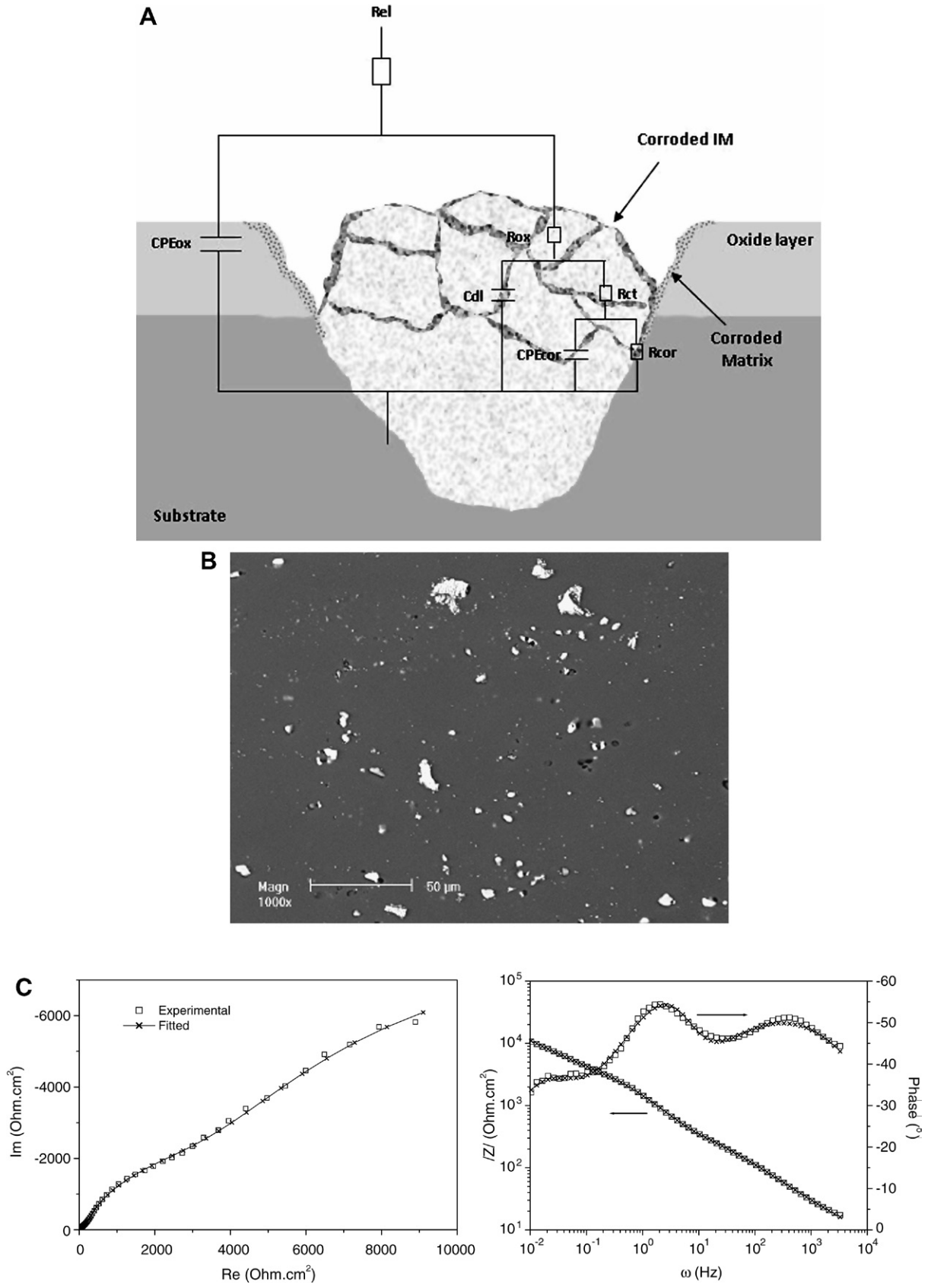

Fig. 12. (A) Equivalent circuit used to interpret EIS data for AA 2024-T3 in 1 mM NaCl solution and its associated physical model; (B) SEM general image of the alloy surface; (C) example of a fitting result for a selected EIS diagram (48.5 h).

showed that the treatment of the high frequency region of impedance diagrams can reveal new features on the electrochemical phenomena taking place at the interface. This treatment is especially relevant for low conductivity electrolytes, such the one used in the

Table 2
Estimates of the equivalent circuit elements for AA 2024-T3 exposed to 1 mM NaCl solution

	Time (h)											
	7.4	11	14	18	24.5	31.5	35	42	45	48.5	55.5	62
Rox Ωcm^2	600	585	568	519	522	540	572	650	707	819	1090	1240
Rct $k\Omega cm^2$	8.0	12.0	11.4	8.4	7.2	6.6	6.7	5.7	6.2	5.6	5.7	5.1
Rcor $k\Omega cm^2$	46.0	36.0	26.5	17.7	46.5	19.9	25.0	11.8	28.9	18.7	20.6	33.5
CPEox $\mu F cm^{-2} s^{(\alpha-1)}$	164	194	194	188	186	170	170	155	154	148	143	130
Cdl $\mu F cm^{-2}$	20.0	23.3	26.1	29.6	34.4	36.3	35.5	32.8	32.3	29.6	24.3	23.7
CPEcor $\mu F cm^{-2} s^{(\alpha-1)}$	211	272	194	475	186	559	545	605	544	566	566	487
α(ox)	0.55	0.52	0.54	0.55	0.57	0.59	0.59	0.61	0.62	0.62	0.63	0.65
α(corr)	0.85	0.93	0.90	0.82	0.70	0.75	0.73	0.79	0.74	0.76	0.79	0.73
Chi-squared ($\times 10^3$)	1.7	0.32	0.40	0.44	0.43	0.53	0.68	0.53	0.56	0.54	0.81	0.49

present study: $9.4 \times 10^{-5} S cm^{-1}$, when the electrolyte resistance can hinder some HF features of the diagrams.

Fig. 11C and D present the evolution of the alloy impedance with immersion time. In these diagrams, the electrolyte resistance contribution was eliminated. To allow comparison, the diagram of Fig. 11A was also included in this new set of diagrams. During the whole test period (approximately 65 h), hardly any change was verified in the impedance modulus and in the Nyquist plots, confirming that the matrix is only slightly attacked by the test electrolyte, as already suggested by the polarization curves presented in Fig. 10, which can be ascribed to the low aggressiveness of the test medium. On the other hand, Bode phase angle diagrams, Fig. 11D, clearly show the existence of three time constants in the investigated frequency range. Analysis of these diagrams shows that the capacitive characteristic of the high frequency (HF) time constant increases with time, while its phase angle maximum is shifted to lower frequencies. On the other hand, the two time constants at lower frequencies are only slightly affected by the exposure time to the electrolyte.

To have a more quantitative evaluation of the EIS response, an equivalent circuit (EC) was used to fit the experimental data. The circuit is presented in Fig. 12A, together with its physical model. In the Figure, a general image of the alloy surface is also presented, Fig. 12B, together with a representative fitting of a selected diagram, Fig. 12C. The overall results of the fitting procedure for diagrams obtained up to 62 h are presented in Table 2. The comparative diagrams presented in Fig. 12C and the low chi-squared values for all the diagrams, Table 2, indicate that the proposed EC is adequate to fit the experimental data. In addition, it is worth to emphasize that the errors involved in the estimates were almost always inferior to 10%, with the highest errors occurring in the low frequency (LF) domain, and only when stronger dispersion of the experimental data was verified.

In the proposed EC the pair Rox//CPEox represents the response of the defective oxide layer. As already shown in the microstructural characterization, and is strongly evidenced in Fig. 12B, there is a great number of IMs in the alloy microstructure. Taking into account these facts, and considering the frequency range at which the HF time constant appears (between 10 kHz and 100 Hz), it might be ascribed to an oxide layer with many flaws, corresponding mainly to the IM particles sites. The value of the CPE exponent (αox) close to 0.5 suggests that the AA 2024-T3 behaves as a porous electrode, which pores would be these weak spots (mostly IMs and their surrounding matrix). As the immersion time increases, the IMs selectively dissolve. They become richer in their more noble constituents, and oxygen-rich products are formed on their surface, as evidenced in the EDS analyses. This could be perceived as the oxide layer healing, as it is very unlikely that EIS measurements could differentiate between the characteristics of the oxide layer formed on the matrix from that formed on the IMs. This might explain the increase in the capacitive response (decreasing capacity values) associated to the HF time constant for longer immersion periods (more than 14 h), as well as the progressive increase in the CPE exponent (αox). Accordingly, the general trend shows an augmentation in Rox values, indicating the diminution of the contribution of these defectives regions (very active IMs) to this time constant response. The anodic polarization curves presented in Figs. 9 and 10 give support to this reasoning. It is worth to emphasize that, regarding the physical interpretation of the time dependent response of this time constant, it seems to be a delicate equilibrium between the oxide layer formed on the bulk alloy, which is only slightly sensitive to the presence of the low chloride content, and the extremely active IMs and their surrounding matrix, which are abundant in this alloy microstructure. Finally, the slow action of the aggressive species towards the oxide-covered alloy should explain the progressive displacement of the phase angle maximum to lower frequencies for longer tests periods.

The fitting response of the pair Rox//Cox during immersion periods' equivalents to those presented in Fig. 9, *i.e.* up to 14 h, is in very good agreement with the interpretation of the polarization curves and with the microstructural characterization. During these first hours, characterized by a strong electrochemical activation of the IMs, there is a decrease in Rox associated with an increase of Cox, both of them indicative of a progressive activation of electrochemically inactive particles.

The MF time constant in the diagrams of Fig. 11, represented by the pair Rct//Cdl in the EC of Fig. 12A, is ascribed to the charge transfer reactions taking place at the interface of the bulk matrix in the defective sites of the oxide layer (mostly near IMs). This assumption is further reinforced by the almost invariant capacity value close to $25 \mu F cm^{-2}$, which is typical of a double layer capacity. With increasing exposure times there is a small decrease in Rct, which is likely due to the action of the chloride ions towards the oxide layer, weakening its protection and increasing the active area.

Finally, the lower frequency time constant, Rcor//Ccor, is associated with the corrosion phenomena occurring in the alloy matrix, mainly at the vicinity of the Cu-enriched IMs. In this frequency region, the experimental impedance data were characterized by a strong dispersion, which is reflected in the oscillation of Rcor in Table 2. On the other hand, Ccor constantly increases, indicating an acceleration of the interfacial process. Accordingly there is a decrease of αcor, which, in the beginning of the exposure period is superior to 0.8, indicating an almost capacitive response, towards a diffusive response, which is typical of pitting corrosion [38,39] that will surely occur at even longer immersion periods.

4. Conclusions

In the present work the microstructure and the corrosion behaviour in low concentrated chloride solution of AA 2024-T3 was investigated. The results of the microstructural survey performed

by TEM confirmed the inhomogeneous nature of the IMs, and evidenced the co-existence of regions with different compositions within the same IM, which may play an important role in their susceptibility to internal corrosion. Moreover, the SEM/EDS results and PSIM images have confirmed the selective dissolution of both S-phase and Al–Cu–Fe–Mn–(Si) IMs, which seems to be a major requirement for the onset of localized corrosion in the Al matrix near the IMs.

Electrochemical results showed that, under the conditions employed in the present study (low chloride concentration), during the first hours of immersion the corrosion behaviour of AA 2024-T3 is dominated by the electrochemical activity within the IMs. In this way, for this time span, the polarization response reflects the activity near and/or within these microstructural features. On the other hand, as the exposure time increases the electrochemical response of the bulk alloy dominates the polarization response, and a passive range starts to appear in the anodic polarization curves.

The results obtained in this work also showed that, in the conditions employed in the present work, untreated EIS diagrams are insensitive to the evolution of the interfacial phenomena occurring with AA 2024-T3; however, the adequate treatment of the HF region of EIS diagrams revealed new features of the fast electrochemical processes taking place on the electrode surface, particularly the changes in the oxide layer response, showing that, when adequately analysed, traditional EIS can be a useful tool to follow the evolution of the corrosion response of AA 2024-T3 due to IM dissolution.

Acknowledgements

The authors are thankful to FAPESP (São Paulo state research-financing agency) for the Grant and for financial support to the project, and to CAPES and CNPq (Brazilian research-financing agencies) for the Grants. H. G. de Melo is thankful to CIRIMAT (Toulouse-France) for the microscopy and impedance facilities.

References

[1] ASM Handbook, Properties and Selection: Nonferrous Alloys and Special-Purpose Materials, 10th ed., ASM International Committee Handbook, vol. 2, 1992, 1328p.
[2] R.G. Buchheit, R.P. Grant, P.F. Hlava, B. Mckenzie, G.L. Zender, J. Electrochem. Soc. 144 (8) (1997) 2621–2628.
[3] S.C. Wang, M.J. Starink, Acta Mater. 55 (2007) 933–941.
[4] V. Radmilovic, R. Kilaas, U. Dahmen, G.J. Shiflet, Acta Mater. 47 (15) (1999) 3987–3997.
[5] C. Genevois, D. Fabrégue, A. Deschampsa, W.J. Poole, Mater. Sci. Eng. A 441 (2006) 39–48.
[6] A. Barbucci, P.L. Cabot, G. Bruzzone, G. Cerisola, J. Alloy. Compd. 268 (1998) 295–301.
[7] A. Barbucci, G. Bruzzone, M. Delucchi, M. Panizza, G. Cerisola, Intermetallics 8 (2000) 305–312.
[8] P. Campestrini, Ph.D. Theis, TUDelft, The Netherlands, 2002, 247p.
[9] C. Blanc, B. Lavelle, G. Mankowski, Corros. Sci. 39 (3) (1997) 495–510.
[10] V. Guillaumin, G. Mankowski, Corros. Sci. 41 (1999) 421–438.
[11] T. Suter, R. Alkire, J. Electrochem. Soc. 148 (1) (2001) B36–B42.
[12] G.S. Chen, M. Gao, R.P. Wei, Corrosion 52 (1) (1996) 8–15.
[13] C.-M. Liao, J.M. Olive, M. Gao, R.P. Wei, Corrosion 54 (6) (1998) 451–458.
[14] Z. Szklarska-Smialowska, Corros. Sci. 41 (1999) 1743–1767.
[15] C. Blanc, S. Gastaud, G. Mankowski, J. Electrochem. Soc. 150 (8) (2003) B396–B404.
[16] G.O. Ilevbare, O. Schneider, R.G. Kelly, J.R. Scully, J. Electrochem. Soc. 151 (8) (2004) B453–B464.
[17] N. Birbilis, R.G. Buchheit, J. Electrochem. Soc. 152 (4) (2005) B140–B151.
[18] P. Schmutz, G.S. Frankel, J. Electrochem. Soc. 145 (7) (1998) 2295–2306.
[19] R.G. Buchheit, J. Electrochem. Soc. 142 (11) (1995) 3994–3996.
[20] P. Schmutz, G.S. Frankel, J. Electrochem. Soc. 145 (7) (1998) 2285–2295.
[21] Danqing Zhu, Wim J. van Ooij, Corros. Sci. 45 (2003) 2163–2175.
[22] H.M. Obispo, L.E. Murr, R.M. Arrowood, E.A. Trillo, J. Mater. Sci. 35 (2000) 3479–3495.
[23] P. Leblanc, G.S. Frankel, J. Electrochem. Soc. 149 (6) (2002) B239–B247.
[24] P. Campestrini, H. Terryn, A. Hovestad, J.H.W. de Wit, Surf. Coat. Technol. 176 (2004) 365–381.
[25] M.A. Alodan, W.H. Smyrl, J. Electrochem. Soc. 144 (10) (2002) L282–L284.
[26] R.G. Buchheit, R.K. Boger, M.C. Carroll, R.M. Leard, C. Paglia, J.L. Searles, JOM July (2001) 29–36.
[27] R.R. Leard, R.G. Buchheit, Mater. Sci. Forum 396–402 (2002) 1491–1496.
[28] O. Schneider, G.O. Ilevbare, J.R. Scully, R.G. Kelly, J. Electrochem. Soc. 151 (8) (2004) B465–B472.
[29] V. Guillaumin, P. Schmutz, G.S. Frankel, J. Electrochem. Soc. 148 (5) (2001) B163–B173.
[30] F. Andreatta, H. Terryn, J.H.W. de Wit, Electrochim. Acta 49 (2004) 2851–2862.
[31] F. Andreatta, H. Terryn, J.H.W. de Wit, Corros. Sci. 45 (2003) 1733–1746.
[32] M. Buchler, J. Kerimo, F. Guillaume, W.H. Smyrl, J. Electrochem. Soc. 147 (10) (2000) 3691–3699.
[33] J.C. Seegmiller, D.A. Buttry, J. Electrochem. Soc. 150 (9) (2003) B413–B418.
[34] Stanley L. Fleger, John W. Heckman Jr., Karen L. Klomparens, Scanning and Transmission Electron Microscopy an introduction Center for Electron Optics, Michigan State University, W.H. Freeman and Company, New York, 1993.
[35] M. Gao, C.R. Feng, R. Wei, Metall. Mater. Trans. A 29A (1998) 1145–1151.
[36] R.P. Wei, C.-H. Liao, M. Gao, Metall. Mater. Trans. A 29A (1998) 1153–1160.
[37] A. Munitz, A. Zangvil, M. Metzger, Metall. Trans. A 11A (1980) 1863–1868.
[38] H. Shih, F. Mansfeld, Corrosion 45 (1989) 610.
[39] A. Conde, J. de Damborenea, Corros. Sci. 39 (2) (1997) 295–303.
[40] D. Ornek, A. Jayaraman, T.K. Wood, Z. Sun, C.H. Hsu, F. Mansfeld, Corros. Sci. 43 (2001) 2121–2133.
[41] G. Baril, C. Blanc, N. Pébère, J. Electrochem. Soc. 148 (12) (2001) B489–B496.
[42] pp. 357–365 P.B. Hirsch, A. Howie, R.B. Nicholson, D.W. Pashley, M.J. Whelan, Electron Microscopy of Thin Crystals, Butterworths, London, 1967 pp. 357–365.
[43] K.A. Yasakau, M.L. Zheludkevich, M.G.S. Ferreira, Suppression of copper redeposition by RE salts and organic complexants as effective tatics of localized corrosion inhibition on AA2024, in: Ninth Symposium on Electrochemical Methods in Corrosion Research, 2006, p. 29.
[44] J.-B. Jorcin, M.E. Orazem, N. Pébère, B. Tribollet, Electrochim. Acta 51 (2006) 1473–1479.